Supplementary Materials for

Induced giant piezoelectricity in centrosymmetric oxides

D.-S. Park *et al.*

Corresponding authors: D.-S. Park, dspark1980@gmail.com; D. Damjanovic, dragan.damjanovic@epfl.ch

Science **375**, 653 (2022)
DOI: 10.1126/science.abm7497

The PDF file includes:

Materials and Methods
Supplementary Text
Figs. S1 to S17
References

Materials and Methods

Film deposition: CGO (thickness of ~1.25 – ~1.80 μm) and YSZ (thickness of ~0.3 μm) films were deposited at room temperature by using an RF magnetron sputtering (RF power: 200W, Ar gas flow: 15 sccm, and working pressure: 1 - 2 × 10^{-2} mbar) and a pulsed laser deposition (a 248 nm KrF Excimer laser, laser fluence: ~2 J/cm^2, repetition rate: 3 Hz, and working pressure: ~1 × 10^{-6} mbar). CGO (Gd: 20 %) and YSZ (Y: 8 %) ceramic targets were used for film deposition. Bottom Al electrodes (100 - 150 nm) on SiO_2 (200 nm)/Si(100) substrates were deposited using a DC sputter prior to film deposition, and top electrodes, Pt/Cr (Pt: ~100 nm and Cr: 10 nm) and Al (~150 nm), were deposited after film deposition. Microstructural properties, crystal structure, and elemental composition of the deposited polycrystalline films were determined by X-ray diffractometer (Bruker D8 advanced x-ray diffractometer, x-ray wavelength: $\lambda = 1.54056$ Å), atomic force microscopy (Cypher VRS), transmission electron microscopy (Double Cs-corrected ThermoFisher Scientific Titan Themis 60-300), and energy dispersive x-ray spectroscopy (EDX) performed at 200kV in the ThermoFisher Scientific Osiris microscope equipped with a Super-X detector at the EMAT laboratory. In the chemical analysis of the sputtered CGO films, Cr impurities of < 5 % were observed (error range of 1 - 2 %). To clarify the influence of such an impurity effect on the electromechanical properties of CGO, we deposited ~350 nm-thick CGO films on the same Al (100 nm)/SiO_2/Si substrates at RT using a pulsed laser deposition (PLD) technique. We confirm the large induced piezoelectric effect in the PLD-deposited CGO films without Cr/other impurities. Note that Cr^{+3} and other acceptor dopants would, like Gd, create Vo in the film. (Fig. S15).

Electromechanical characterizations: Electric field-mechanical displacement responses of the films were recorded by implementing an advanced linear variable differential transformer (LVDT) and fiber-optic measurements. The LVDT sensor consists of a stationary element (including a primary magnetic coil, secondary coils symmetrically spaced with respect to the primary coil, and a movable core). Flat and hemispherical sample stages were electrically grounded. The LVDT sensor was equipped with two commercial lock-in amplifiers (SR830 DSP), a voltage source meter (Stanford Research System, Model No. DS360), and a voltage amplifier (Trek, Model No. 609c-6). The voltage source meter was used to apply AC voltages or combined AC & DC voltages to the samples. The two lock-in amplifiers are separately connected to drive LVDT and to measure output signal amplitudes (and an oscilloscope is used to display output signals). The output signals were converted to mechanical displacement via the calibrated instrument sensitivity (1.55 × 10^{-6} m/V). In the photonic sensing system (MTI-2100 Fotonic Sensor), samples were mounted on an alignment stage and displacements were measured from the reflective sample surface (grounded top electrode) in noncontact mode. Electric voltage was applied to the bottom electrode, connected with a lock-in amplifier and a voltage source meter. Photonic sensor has a linear voltage response to a change of sample -sensor distance. The effective probe area is approximately 0.79 mm^2 and an instrument sensitivity was 7.565 × 10^{-6} m/V. During displacement measurements in both of the above systems, all of the real-time output amplitude signals were concurrently recorded by using an oscilloscope (Tektronix, MDO3014). Prior to sample measurements, external instrument offset voltages, electrical noise, and instrumental sensitivity were corrected and confirmed by measuring reference samples, e.g. standard quartz crystal and PZT samples, in both of the systems.

Supplementary Text

Section 1: Determination of harmonic electromechanical susceptibility.

In this work, the first harmonic electromechanical strain (x_{33}) and piezoelectric susceptibility (d_{33}) of the samples in out-of-plane capacitor geometry were defined as:

$$x_{33} = \Delta L/L = d_{33}E_3, \tag{1.1}$$

where ΔL is the electromechanical displacement along film thickness, L, and E_3 is the applied electric field. The d33 is calculated as:

$$d_{33} = \Delta L/V_{in} = [V_{out}\xi]/V_{\mathrm{in}}, \tag{1.2}$$

where V_{out} is the measured displacement amplitude in volt, ξ is the instrument sensitivity (1.55×10^{-6} m/V and 7.565×10^{-6} m/V for LVDT and photonic sensing system, respectively), and V_{in} is the applied electric voltage amplitude. The piezoelectric coefficient of the first harmonic is expressed by V_{out} and phase lag, φ, in a function of applied frequency, f:

$$d_{33} = \frac{\xi V_{out} e^{i(\omega t-\varphi)}}{V_{in}e^{i\omega t}} = \xi\frac{V_{out}}{V_{in}}e^{-i\varphi} = \xi\frac{V_{out}}{V_{in}}(\cos\varphi - \mathrm{i}\cdot\sin\varphi), \tag{1.3}$$

where $\omega = 2\pi f$ is the angular frequency, t is time, and φ is the phase delay of the output response with respect to the applied AC electric field.

For the electrostrictive response of the samples, the second harmonic electromechanical susceptibility, M_{33} ($\mathrm{m}^2/\mathrm{V}^2$), of the samples in the out-of-plane capacitor geometry were determined as

$$x_{33} = \Delta L/L = M_{33}E_3^2, \tag{1.4}$$

$$M_{33} = \frac{LV_{out}\xi}{V_{in}^2}. \tag{1.5}$$

The induced second-order electromechanical displacements in time is expressed by a function:

$$\Delta L = \frac{M_{33}V_{in}^2\xi}{L}sin^2(\omega t-\varphi). \tag{1.6}$$

$$\Delta L = \frac{M_{33}V_{in}^2\xi}{L}\left[\frac{1}{2}-\frac{1}{2}\cos(2\omega t-2\varphi)\right]. \tag{1.7}$$

Thus, a pure second-harmonic displacement in time is:

$$\Delta L = -\frac{M_{33}V_{in}^2\xi}{2L}\cos(2\omega t-2\varphi). \tag{1.8}$$

For clamped thin films, the thickness strain x_3 is given by the modified M coefficients:

$$x_{33} = [M_{33} - \frac{2s_{31}}{(s_{11}+s_{21})}M_{31}]E_3^2, \tag{1.9}$$

where s_{ij} are components of the elastic compliance tensor of the film and M_{31} transverse electrostrictive coefficient. For simplicity and without a loss of generality, eq. (1.4) is used in this work, with M_{33} representing both contributions between the brackets of eq. (1.9), i.e. the effective M_{33}.

Section 2: Capacitance measurements for the CGO samples

The charge density, D ($\mathrm{C/cm}^2$) was determined from the capacitance C of the sample, as measured in a series RC circuit. The impedance Z of the circuit was excited by an AC voltage $Ve^{i\omega t}$ and the following relations are used for calculation:

$$V = IZ, \tag{2.1}$$

$$Z = R_{ex} + 1/(i\omega C), \tag{2.2}$$

where I is the current, and R_{ex} is the external resistance (10 - 100 Ω) of the series circuit. By substituting eq. (2.1) to eq. (2.2), the output voltage (V_{out}) of the circuit is obtained when a voltage (V_{in}) is applied as:

$$V_{\text{out}} = R_{ex}I = V_{\text{in}}R_{ex}/[R_{ex} + 1/(i\omega C)]. \tag{2.3}$$

Introducing a condition of $R_{ex} \ll 1/(\omega C)$ (see Fig. S3b), the capacitance of the RC circuit can be expressed by

$$C = V_{\text{out}}/(V_{\text{in}}R_{ex}i\omega). \tag{2.4}$$

The capacitance of the samples is described by

$$C = \frac{\varepsilon_0\varepsilon_r A}{L}, \tag{2.5}$$

where ε_0, ε_{r}, and A are the vacuum permittivity and the relative permittivity of the materials, and the measured electrode area, respectively. The total charge density of sample is obtained by combining eqs. (2.4) and (2.5):

$$D = \varepsilon_0\varepsilon_{\text{r}}E = CV_{\text{in}}/A. \tag{2.6}$$

Section 3: Electric field-enhanced ionic defect dynamics and dielectric permittivity

The electric field-induced electrostrictive strain, x, can be expressed as $x = ME^2$. The polarization (P) of the material is induced by the applied E and can be given as $P = \varepsilon E$. Combining the field-induced electrostriction and polarization, the polarization-induced electrostrictive strain can be defined as $x = QP^2$ (*17*).

In the relation $M_{ijmn} = Q_{ijkl}\varepsilon_{km}\varepsilon_{ln}$ it was found that the dielectric constants ε_{nm} of electrostrictive materials, such as, e.g., (0.9)PMN-(0.1)PT, are nonlinear and staturate with applied electric fields. This indicates that M is not constant when ε is field-dependent and dispersive. Such a dependence is indeed observed in this work. Theoretical considerations as well as experiments show that $Q \propto 1/\varepsilon$ and thus $M \propto \varepsilon$. The well-known strong (inorganic) electrostrictive materials do not excel because of a large electrostrictive coefficient Q, but because of a large polarizability. The polarization, induced by an electric field is large, which implies that the derivative $\varepsilon_{ij} = \frac{\partial P_i}{\partial E_j}$, *i.e.*, the dielectric response, may also be large. In order to address the origin of large electro-mechanical properties of CGO (e.g., giant electrostriction and piezoelectricity), it is therefore primordial to indentify the origin of large permittivity and large induced polarization.

CGO has a cubic flourite structure (space group: *Fm*-3*m*) at room temperature and it cannot intrinscially exhibit a spontaneous polarization. The doped ceria, however, has many unit cells with broken symmetry because of the dopants (20 % Gd on cerium sites), the compensating oxygen vacancies (5 % of oxygen sites), and additional oxygen vacancies (y) which stem from a reducing processing step in the material synthesis (*14*). It is believed that the liberated electrons are not entirely free, but some are trapped into the 4*f* states of Ce^{3+}. The complete formula thus must be written in the Kröger-Vink notation as $Ce^{\times}_{0.8-2y}Ce'_{2y}(Gd'_{Ce})_{0.2}O^{\times}_{1.9-y}([V_O^{\bullet\bullet}])_{0.1+y}$. The oxygen vacancies are mobile and the activation energy of their hoppings is about 0.45 – 0.70 eV in undoped CeO_{2-x}., stronlgy dependent on atmospheric conditons and microstructure (*19, 27-30*). This value increases to 0.75 eV in ceria doped with 20 % Gd as the $V_O^{\bullet\bullet}$ are “trapped” close to the Gd point defects (*14*). In addition, the dopants obstruct the easy path in the “*oxygen channels*” due to their larger size. By charge neutrality, there are twice as many Gd point defects as V_O^{+2}. The vacancies obtained by reduction can be trapped by Ce^{+3} up to another 5 % of oxygen sites.

By introducing 20 % Gd into Ce sites, almost every unit cell (u.c.) has an oxygen defect (V_O density of 2.52×10^{21} cm^{-3}). It was found that, in thermal equilibrium (low temperatures below 600 °C), the preferred site of an oxygen vacancy is the next-next neighbour (*n.n.n*) site of Gd (*19,* *27*). If Gd is placed in the coordinate (0,0,0) as in standard unit cell definition, the next oxygen sites are <1/4, 1/4, 1/4>. The n.n.n site are obtained by a basic translation of the fcc lattice, such as (1/2, 1/2, 0) yielding <1/4, 1/4, 3/4>. This next-next neighbor distance, *d*, is 4.48 Å [= 5.4179 Å (a_{bulk}) × 0.829] in CGO (Gd 20 %). Assuming that most vacancies are in such positions, we can identify a high density of dipoles, *qd*, where the charge, *q*, is one unit charge, *e*. Defining the average concentration, *c*, of Gd sites per unit cell to be 0.8 (4 cations per u.c. × 0.2), we obtain a potential total polarization, P_{s}, as:

$$P_{\mathrm{s}} = \frac{c}{2} a^{-3} qd = \ 0.18\ \mathrm{C}/m^2 \qquad (3.1)$$

The orientation of this polarization is not stable and thus must be forced by an external field (E_{DC}). The reorientation of the polarization is effectuated by oxygen ion hopping. The basic polarization reorientation mechanism is based on one or several hops of oxygen vacancies, which require an activation energy of ϕ = 0.32 to 0.75 eV depending on the distance to the next Gd as shown in Fig. S10 (*19*). Typically, we treat this hopping as an ordinary diffusion process in a weak electric field. In the experiements carried out here, the applied large clamping fields are not weak, one has to evaluate the jumping probabilities. We emphasize the possibility explicitely for both directions and/or against the electric field:

$$W(+) = e^{-\phi/kT} e^{+qEh/2kT}, \qquad (3.2)$$

$$W(-) = e^{-\phi/kT} e^{-qEh/2kT}, \qquad (3.3)$$

$$W(\text{forward}) = e^{-\phi/kT}\left(e^{+qEh/2kT} - e^{-qEh/2kT}\right). \qquad (3.4)$$

These probabilities describe the success rate for the jumps attempted υ times per second. The parameter h is the hopping distance, typically by half a lattice constant (~2.7 Å). For the attempt rate, we use a typical phonon frequency of ~10^{11} Hz, which was experimentally determined by means of diffusion studies in other works. In absence of an electrical field, the effective hopping rate at 300 K is:

$$R_0 = \upsilon e^{-\phi/kT}, \qquad (3.5)$$

= 2.5×10^{-2} Hz (ϕ = 0.75 eV) or 400 Hz (ϕ = 0.5 eV) or 13 kHz (ϕ = 0.41 eV)

This implies the corresponding relaxation times, $\tau_0 = 1/R_0$, of 40 s, 2.5 ms, and 76.8 µs, respectively. The effective hopping rate in the direction of an electric field can be written as:

$$R(E) = \upsilon e^{-\phi/kT}\left(e^{+qEh/2kT} - e^{-qEh/2kT}\right). \qquad (3.6)$$

The single polarization average is written by:

$$< p(t) >= qd(1 - e^{-R(E)t}), \qquad (3.7)$$

$$P(\mathrm{t}) = \frac{\frac{c}{2}\left(1 - \frac{c}{2}\right)}{a^3} < p(t) > \qquad (3.8)$$

Using the time-dependent polarization, the dielectric constant can be derived as:

$$\begin{aligned} \varepsilon_r = \frac{\partial P}{\partial E} &= \frac{\frac{c}{2}\left(1 - \frac{c}{2}\right)}{a^3} qde^{-R(E)t} \upsilon te^{-\frac{\phi}{kT}} \frac{qh}{2kT}\left(e^{+\frac{qEh}{2kT}} + e^{-\frac{qEh}{2kT}}\right) \\ &= \frac{\frac{c}{2}\left(1 - \frac{c}{2}\right)}{a^3} \upsilon qde^{-R(E)t} \frac{t}{\tau_0} \frac{qh}{2kT}\left(e^{+\frac{qEh}{2kT}} + e^{-\frac{qEh}{2kT}}\right). \end{aligned} \qquad (3.9)$$

By integrating time, t, over a sinusidal period, $1/f$ or $2\pi/\omega$, eq. (4.8) can be given as:

$$\varepsilon_r = \frac{\frac{c}{2}\left(1 - \frac{c}{2}\right)}{a^3} \upsilon q d \frac{qh}{2kT} \frac{2\pi}{\omega\tau_0} \left(e^{+\frac{qEh}{2kT}} + e^{-\frac{qEh}{2kT}}\right) e^{-R(E)t} \tag{3.10}$$

By introducting parameters, $t = 0$ (far from saturation), T = 300 K, ϕ = 0.41±2 eV (experimentally obtained, see Fig. S10), and c = 0.8, giant dielectric permittivity in CGO (20% Gd) can be induced with lowering frequency as shown in Fig. S10. Our resuls clearly show the dielectric permittivity of CGO strongly relies on the activation energy of ionic defect hopping and its rate (frequency dependence) under the applied E_{DC}. The proposed ionic diffusion model and the corresponding variations in the dielectric permittivity of CGO give excellent agreement with the experimental results. Therefore, we affirm that the static field-enhanced ionic hopping/conduction drives large frequency-dependent dielectric permittivity, which helps generating the correlated large piezoelectricity. Note that this hopping model does not include phase transition and electric field-induced V_O separation on large-scale distance of the CGO films. Therefore, this model is valid for modelling high-frequency dielectric constant, *i.e.*, the value of several hundred measured at 1 kHz.

Section 4. x-ray diffraction measurements with in-situ electric field applications.

Structural variations of the polycrystalline CGO (Gd 20%) films were investigated using in-situ XRD (Bruker D8 advanced x-ray diffractometer, λ (Cu-$K\alpha$ radiation) = 1.54056 Å) under different DC electric fields (0 - 1 MV/cm). The same samples used for our electromechanical tests were measured. The electrode (Pt/Cr) area of the films is about 15 % to the total surface area of the samples. The electric fields were applied from top electrode (Pt/Cr) to bottom electrode (Al) while measuring XRD. To acquire sufficient XRD intensity for the field-induced structural variations of the films, long scan time for each angle step (5 - 10 sec/step) were employed for XRD measurements with fine angle increments (0.005° – 0.01°). All of the collected diffraction spectra were further calibrated by referring to the multiple diffraction of the forbidden Si (200) peak at 2θ = 33° (*31*). The pristine CGO films deposited at room temperature are polycrystalline and predominantly show broad diffraction CGO (111) and (220) peaks at 2θ = 27.49° and 46.12°, respectively. These peak angles of the pristine films are lower than those of ideal CGO (Gd 20%) (2θ = 28.47° and 47.36°). This indicates that the film has a larger lattice constant (5.61 Å) compared to that of bulk CGO (Gd 20%) (5.425 Å). This is due to additional amount of oxygen vacancies in the films around 8 % of oxygen sites (*14*), which can result in the Vo-induced chemical expansion of the pristine film due to the valence change of compensating Ce from Ce^{4+} (97 pm) to Ce^{3+} (114 pm) (*20*).

Remarkably, XRD clearly shows the appearance of a new peak at 2θ = 32.16 when the electric field applied to the sample increases above E_{DC} = +0.8 MV/cm. It is likely that additional peaks appear at 27.78° and 46.03°, but are hidden by overlapping cubic reflections. The peaks may be present at lower fields but are below detection limit. This directly indicates appearance of a field-induced phase transformation in the CGO film. Phase transitions (among three solid polymorphs, cubic (space group Fm-3m), tetragonal ($P4_2/nmc$), and monoclinic ($P2_1/c$) symmetries) have been often observed in fluorites (ZrO_2, aliovalent cation-stabilized ZrO_2, and CeO_2) by controlling doping, temperature and applying large electric field at relatively high temperature (*22, 23, 25, 32*). For example, *Zhu et al.* reported that the effect of V_O in CeO_2 stabilizes a tetragonal phase ($P4_2/nmc$) via charge transfer ($V_O \rightarrow Ce^{3+}$) at temperatures below 100 ^oC (*25*). Hence, V_O-induced phase transition in the CGO films can occur and be promoted when the density of V_O at the cathode increases by high applied DC&AC electric fields. With the tetragonal phase within the CGO film (Fig. S16), we obtained the tetragonal lattice parameters $a_{(T)} = b_{(T)} = 3.94$ Å and $c_{(T)} = 6.41$ Å.

In order to better apprehend this transformation, one has to be aware of the usual set of elementary vectors describing the Bravais FCC lattice. The FCC lattice is a non-primitive cubic lattice. It contains the ones of the primitive unit cell $[\frac{a}{2},\frac{a}{2},0]$, $[\frac{a}{2},0,\frac{a}{2}]$, $[0,\frac{a}{2},\frac{a}{2}]$, spanning the primitive unit cell with one formula unit, and the ones of the cubic frame ([a,0,0], [0,a,0], [0,0,a]), which includes 4 formula units ($Z = 4$, where Z is the number of formula units in the crystallographic unit cell). A tetragonal unit cell can be equally well defined with the base plane spanned by the primitive unit vectors $[\frac{a}{2},\frac{a}{2},0]$, $[\frac{a}{2},-\frac{a}{2},0]$ and the basic translation $[0,0,a]$ along the 4-fold axis perpendicular to the base plane. We still need to add a third primitive unit cell vector $[\frac{a}{2},0,\frac{a}{2}]$. This non-primitive, tetragonal unit cell has $Z = 2$, and half the volume of the standard FCC unit cell (a^3) (*24*). The unit cell dimensions of the observed new tetragonal phase have to be compared with the tetragonal choice of the FCC unit cell axes, *i.e.*, $\sqrt{2}a(\mathrm{t}) = \sqrt{2}b(\mathrm{t}) = 5.57$ Å, $c(\mathrm{t}) = 6.42$ Å. Therefore, the corresponding strains in crystallographic a and c axes are $(\sqrt{2}a_{(T)} - a_{(C)})/a_{(C)} \approx -0.7\%$ and $(c_{(T)} - c_{(C)})/c_{(C)} \approx +14.5\ \%$, respectively.

Section 5. Frequency dependence of *d* and *M*

Three points need to be recalled for ensuing discussion. First, materials coefficients are derivatives of strain, and polarization ($\varepsilon = \partial P/\partial E, d = \partial x/\partial E,\ Q = \frac{1}{2}\partial^2 x/\partial P^2$); therefore, it is the change of polarization and strain with field that matters for a large response and not their absolute values. Second, the field induced transformation into tetragonal phase is partial, i.e., during application of the field of sufficient magnitude and after sufficient time, the sample exhibits mixed cubic and tetragonal phases. Third, the field induced phase transformation appears to be reversible.

During electrostrictive measurements (Fig. 1 in the main text), only moderate E_{AC} is applied. This field can at best cause partial phase transformation and associated strain near the field peak, when E_{AC} reaches critical field needed for phase transformation, as the field is cycled between $-E_{AC}$ and $+E_{AC}$. At frequencies above ~10 Hz, the phase transformation is limited under assumption that it is assisted or enabled by V_O migration because defects cannot follow the field easily. The electrostriction coefficient M is then essentially controlled by ε and Q of the cubic phase, both of which are mostly due to the intrinsic contribution and some polarization due to the limited field-induced charge migration and hopping. As the frequency decreases, motion of V_O becomes more pronounced, contributing both to ε and to the strain from the phase transformation. This process defines the rate-dependent electrostrictive coefficient.

On the other hand, piezoelectric measurements are made under strong E_{DC} and a small E_{AC}. Under E_{DC} of sufficient strength, the sample consists at all times of a mixture of tetragonal and cubic regions. Under E_{DC} the energy barrier among these regions must be low, so that even a relatively weak E_{AC} fields can reversibly switch between the cubic and tetragonal phases in some volume fraction of the sample, if enough time is given for displacement of V_O that increases susceptibility for the transformation. This was directly observed by a concurrent measure of $|d_{33}|$ and $|M_{33}|$ under a high E_{DC} as shown in Fig. 3D. At frequencies above about ~10 Hz, the weak E_{AC} cannot move V_O fast enough to promote further oscillating phase transformations. The field-induced d is thus governed by the values of Q and ε, which are representative of the mixture of the cubic and tetragonal phases. The polarization electrostrictive coefficient and permittivity are not expected to change much (less than an order of magnitude) between different phases (*33*). This means that in this high frequency range the *d* coefficient is essentially controlled by the same intrinsic relationships as *M*, leading to a good agreement between the measured *d* and the value estimated from $2ME_{\mathrm{DC}}$. The small discrepancy between expected and measured values at high frequency (1 kHz) can be explained by the differences in values of the *Q* coefficients in the tetragonal and cubic phase and weak extrinsic contributions to ε, which will be different under conditions used for measuring *d* and *M*. At low frequencies, the rate of change of field is slow enough that motion of V_O can help reversible cubic-to-tetragonal (and back) transformation during E_{AC} cycling, leading to a huge contribution to the apparent piezoelectric strain.

Furthermore, the direct longitudinal piezoelectric effect ($D_3 = d_{33}\sigma_3$ or $E_3 = -g_{33}\sigma_3$, where σ and *g* are applied pressure and direct piezoelectric voltage coefficient, respectively) (*34*) should be measurable by application of a dynamic pressure once the required fundamental condition, macroscopic symmetry breaking is achieved by externally applied direct electric field E_{DC}. Such an experiment requires measurements of either small *D* (*d* coefficient) or small *E* (*g* coefficient) in presence of a large E_{DC} while simultaneously applying dynamic stress. The stress may also interfere with the conditions needed to achieve the phase transition.

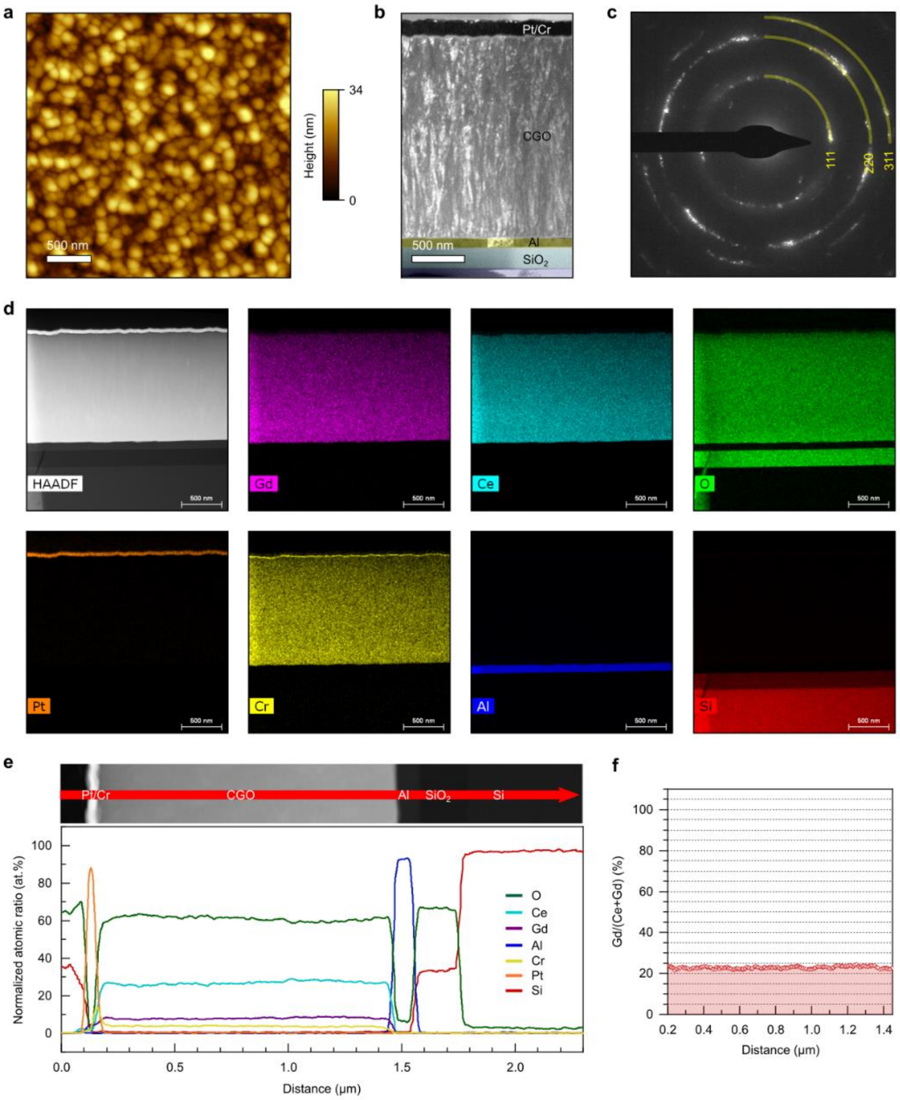

Fig. S1. Surface morphology, microstructural properties, elemental mappings, and line profiles of CGO film samples. (a) Atomic force microscopy topography image (3 × 3 μm^2) of the surface of a CGO film. **(b)** A cross-sectional dark field transmission electron microscopy image of the Pt/Cr/CGO (~1.8 μm-thick)/Al/SiO_2/Si sample. **(c)** Electron diffraction patterns of the polycrystalline CGO film. **(d)** EDX elemental mapping of a CGO film (~1.25 μm-thick) sample. For comparison, the EDX mapping images of different elements (Gd, Ce, O, Pt, Cr, Al, and Si) are presented separately. **(e)** EDX line profiles of the CGO film sample along the arrow, shown in the top cross-sectional high-angle dark field scanning transmission electron microscopy image. **(f)** The atomic ratio of Gd to Ce in the CGO film, determined to be 22.8±1.6 %. According to the EDX analysis, Cr impurities (~2 %) were found in the film layer, of which such contaminants are from deposition tools/external mechanical processing.

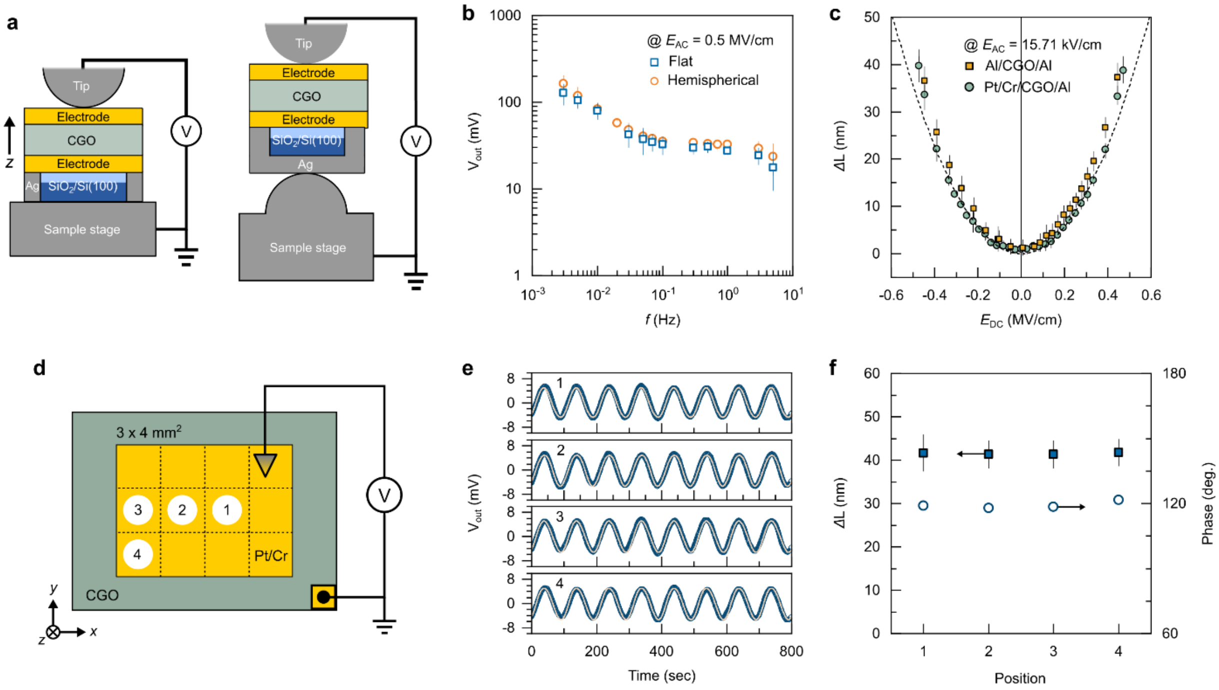

Fig. S2. Verification of measurement artifacts. (**a**) Schematics of different sample clamping methods for the sample measurements in LVDT. Two different sample stages, flat and hemispherical stages, were employed. A radius of the hemispherical sample stage is 2.5 mm, smaller than any of samples measured. (**b**) Out-of-plane displacement amplitudes (V_{out}) of the CGO samples as a function of frequency, determined by separately using the flat and hemispherical metal stages. (**c**) Variations in the first-order electromechanical displacements of the CGO films with different top electrodes (Pt/Cr and Al), excited by simultaneously applying E_{AC} = 15.71 kV/cm and E_{DC} = +0.5 MV/cm. This indicates there is no significant asymmetric Schottky effect for the generation of large electromechanical responses of CGO films. (**d**) Schematic of different probe points on a CGO sample for mechanical measurements in the photonic sensing system. Samples were firmly mounted on a flat metallic stage by Ag paste. Top (Pt/Cr or Al) electrodes were connected by a metal tip and the electrical fields were applied between the top and bottom (Al) electrodes. Electromechanical displacements for four different probe points (photonic sensor positions, denoted as 1, 2, 3, and 4) were measured while fixing the tip contact under a constant electric bias apply (E_{AC} = 15.71 kV/cm & E_{DC} = -0.5 MV/cm). (**e,f**) The measured displacements and phase response of the probe points as a function of time and probe point position. By comparing results obtained for two measurement setups, we confirm that substrate bending is suppressed by gluing the sample to the flat stage, thus having no substantial effect on electromechanical measurements.

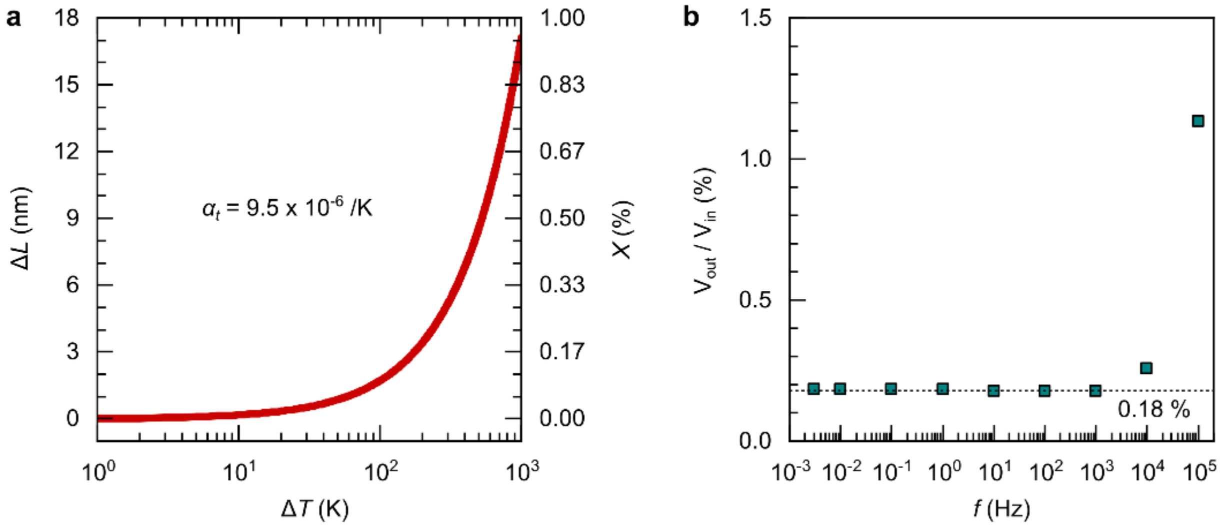

Fig. S3. Expected thermally induced volumetric strain effect in CGO (Gd 20 %) and external resistor effect in series RC circuit. (a) The thermal expansion of CGO films is predicted by a linear formula, $X = \Delta L/L = \alpha_t(\Delta T)$, where α_t and T are the thermal expansion coefficient (9.5×10^{-6} K^{-1}) for the case of CGO (Gd 20 %) and temperature change, respectively (*35*). A temperature increase of < 40 °C was found during high-field applications (E_{DC} ~0.8 MV/cm at 10 mHz) by directly attaching a thermocouple to the surface of the sample. **(b)** Output voltage (V_{out})/input voltage (V_{in}) ratio as a function of frequency during the electrical measurements. An external resistor, R_{ex}, is added in series with the sample and voltage drop (V_{out}) is measured across R_{ex} to determine electrical current and electro-mechanical responses of the sample. As the current across R_{ex} can be a strong function of frequency, V_{out} can also show a strong frequency dependence. To eliminate this effect, a constant very low V_{out}/V_{in} ratio ($\omega R_{ex}C \ll 1$ %) was kept during the concurrent electrical and electromechanical measurements.

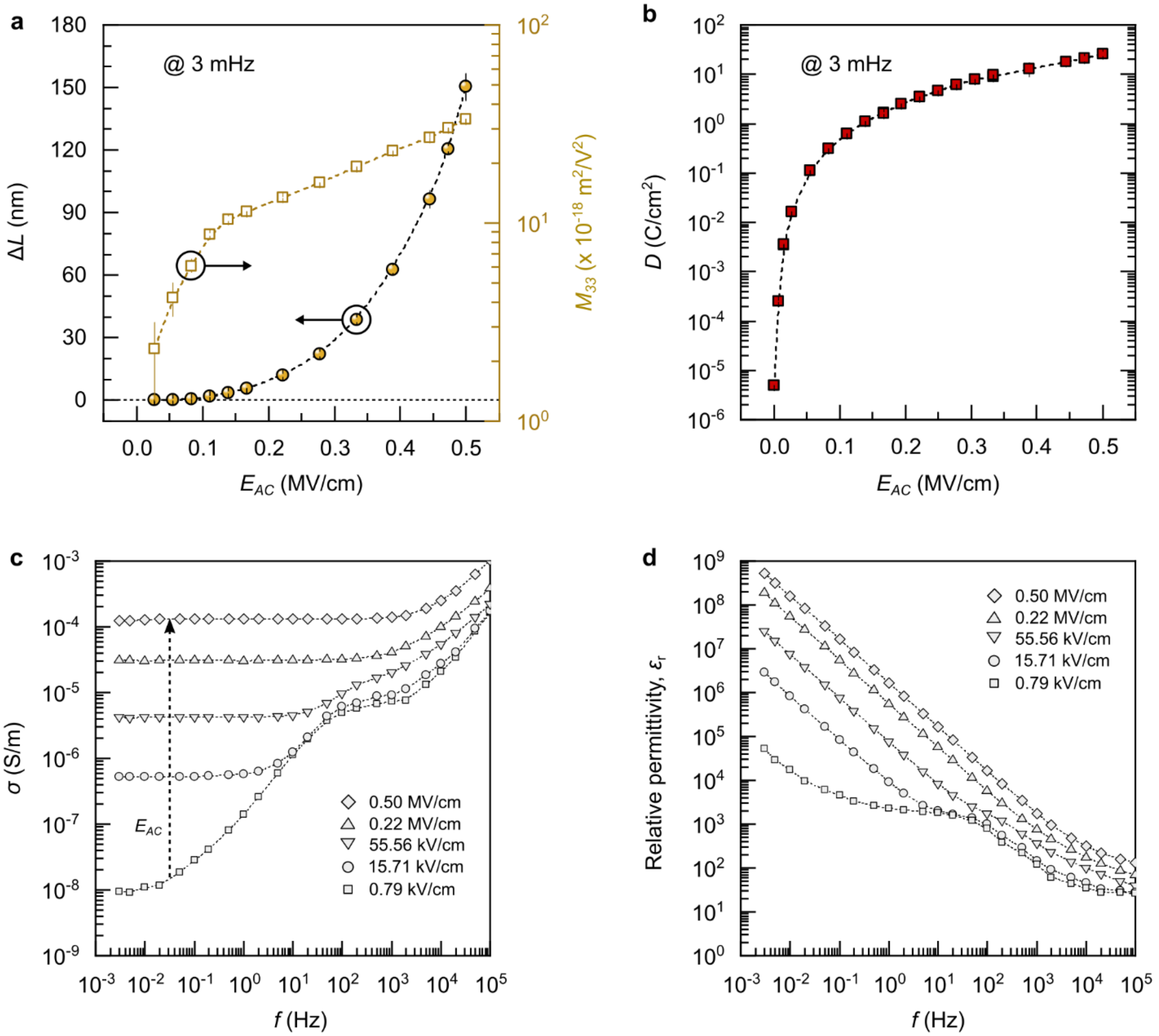

Fig. S4. Variations in the electrostrictive response, charge density, conductivity, and dielectric permittivity of the CGO film as functions of applied E_{AC} and frequency f. (a) The second order electromechanical displacements, ΔL, and susceptibility, M_{33}, of the CGO film with E_{AC} at $f = 3$ mHz. A large increase in the low-frequency M_{33} of the film occurs when E_{AC} increases. **(b)** The corresponding change in the charge density, D, of the film with E_{AC}. **(c)** The f-dependent electrical conductivity of the sample as a function of E_{AC}. **(d)** The relative dielectric permittivity of the CGO film as a function of E_{AC} and f.

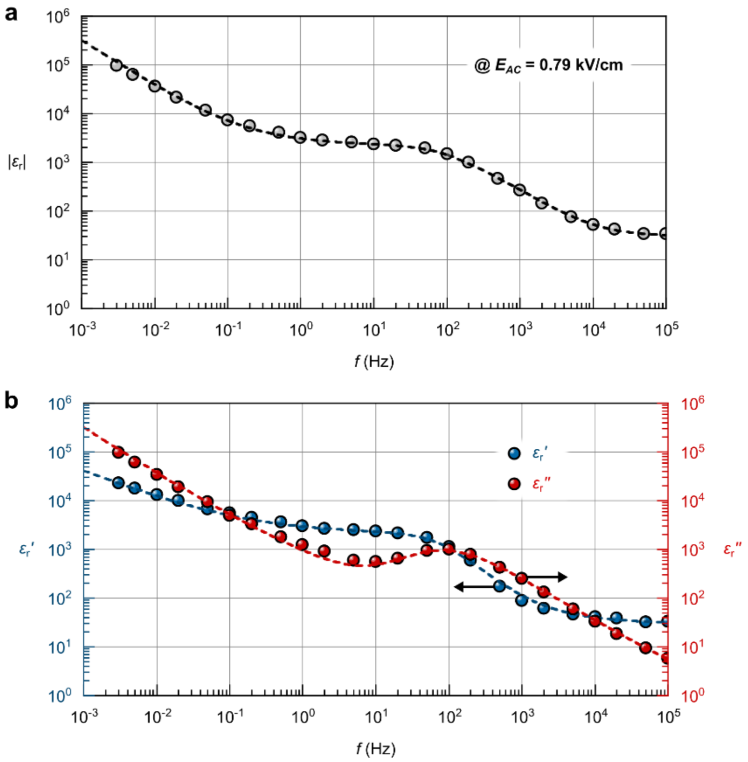

Fig. S5. Complex apparent dielectric permittivity and relaxation characteristics of the CGO film. (a) Modulus $|\varepsilon_\mathrm{r}| = \sqrt{\varepsilon_\mathrm{r}'^2 + \varepsilon_\mathrm{r}''^2}$ of the apparent relative dielectric permittivity of the CGO film as a function of *f*, excited by E_AC = 0.79 kV/cm. The experimental dielectric permittivity (circles) were fitted by a modified complex dielectric relaxation model (dashed lines) incorporating multiple relaxation processes and the conductivity terms (*36*). **(b)** The real (ε') and imaginary (ε'') parts of the permittivity of the CGO film. The magnitudes of the ε' and ε'' significantly increase with decreasing *f*.

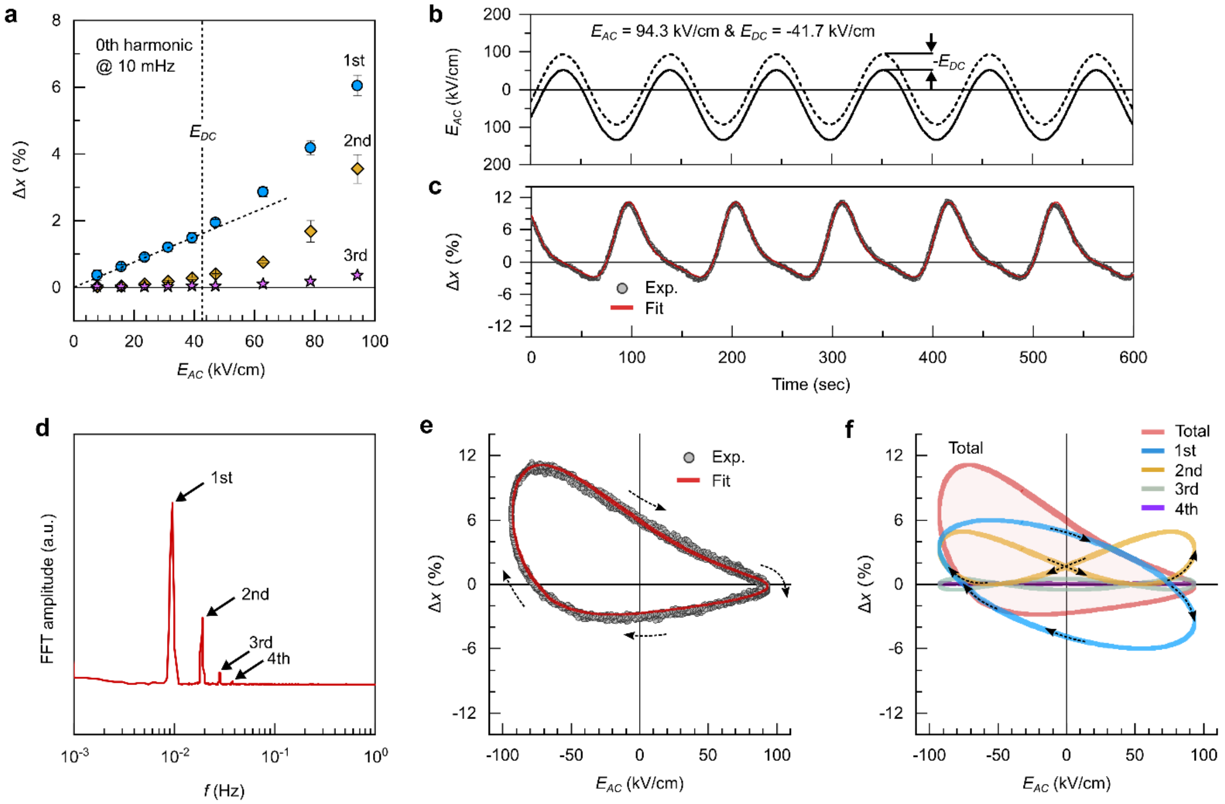

Fig. S6. Nonlinear electromechanical responses of CGO film. (a) The first, second, and third harmonic electromechanical strains of the film as a function of E_{AC}, measured at 10 mHz. **(b)** Applied combined E (E_{AC} = 94.3 kV/cm and E_{DC} = -41.7 kV/cm) to the sample at f = 10 mHz. **(c)** Spectral analyses of the measured strain (grey circle) of the film, fitted by multiple sinusoidal functions (red solid line), $x_{\mathrm{Tot.}} = \Sigma\ x_{0,n}\sin(n\cdot\omega t - \varphi)$. **(d)** FFT analysis for the measured electromechanical signals in frequency. **(e)** Strain versus E_{AC} curve of the CGO film under E_{DC} (-41.7 kV/cm). **(f)** A spectral analysis of strain distribution in the film during the field application, fitted by combining four (first to fourth) harmonic components. Such high-order harmonics originate from the nonideal electrostriction in CGO (and most other materials) where the associated total ideal quadratic strain, $x = ME^2$ can be modified by expressing the coefficient M as being field dependent, $M = m + nE + pE^2 + \cdots$, thus giving $x = mE^2 + nE^3 + pE^4 + \cdots$ (*17*). Also, asymmetric/nonlinear strain versus electrical field responses can be generated by instrumental voltage offsets and thus careful instrumental calibration is always required for sample measurements.

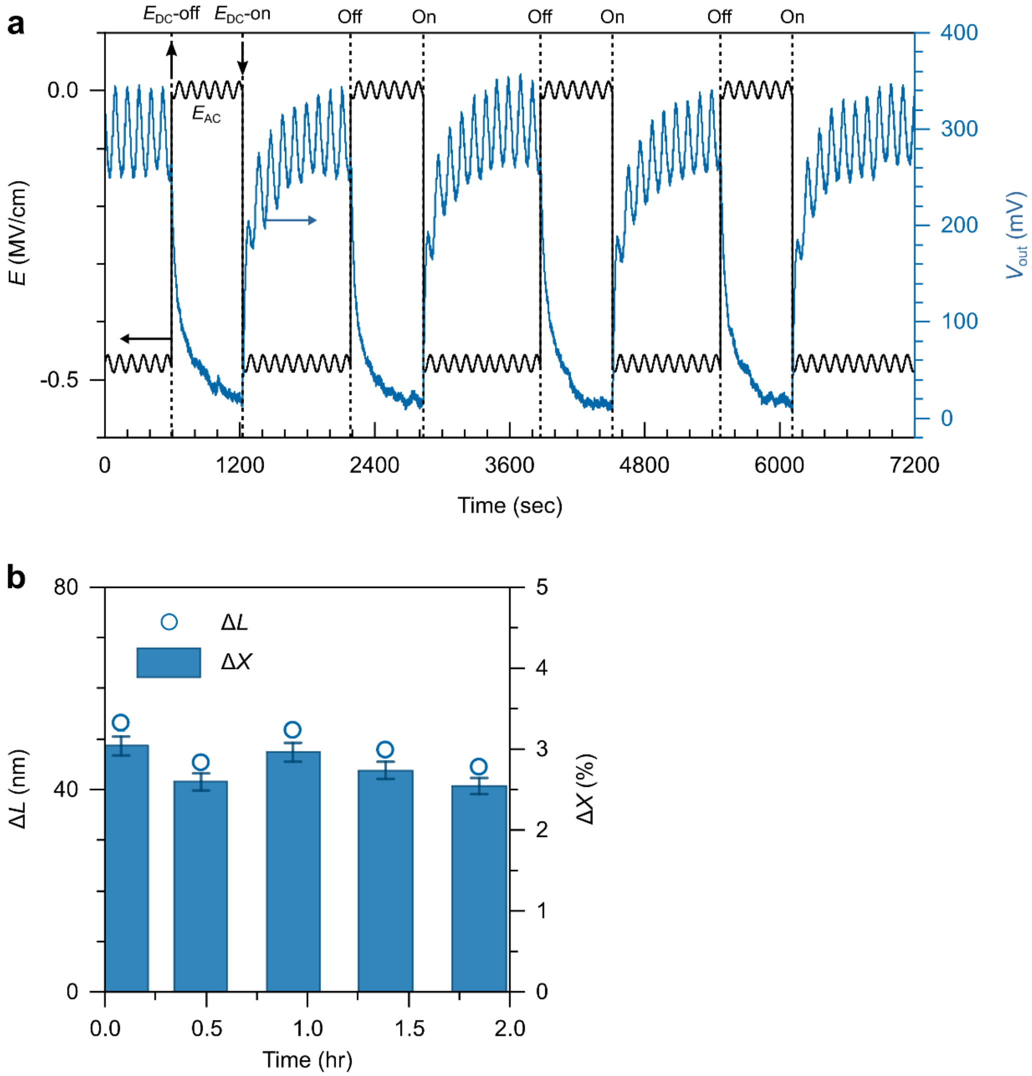

Fig. S7. On-off control of the first harmonic electromechanical responses of the CGO film by simultaneously applied DC field. (a) The first-order harmonic displacement amplitude (V_{out}) of the CGO film as a function of time. The output amplitude is switched by on-and-off negative DC field (E_{DC} = -0.5 MV/cm) while applying a constant AC field (E_{AC} = 15.71 kV/cm). **(b)** The corresponding electromechanical displacements and strain of the film as a function of time.

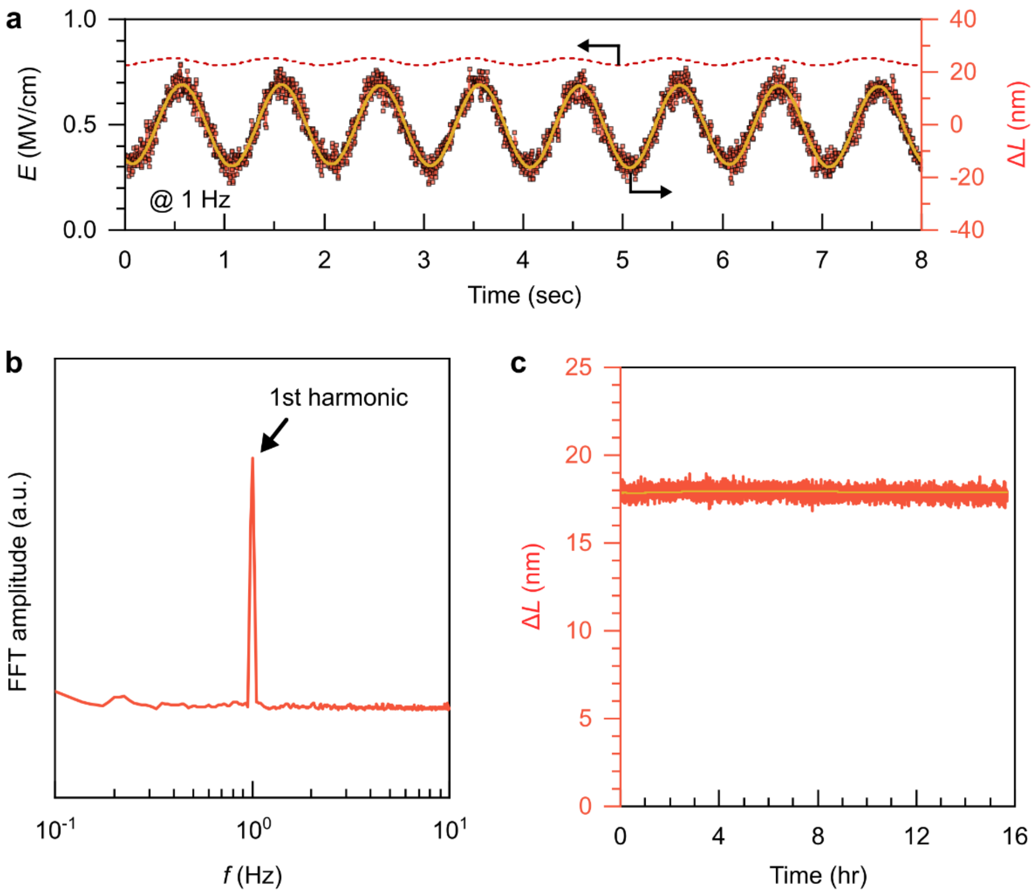

Fig. S8. Endurance performance on the induced piezoelectric displacement of the 1.25 μm-thick CGO film. (a) The piezoelectric displacement (max. the first harmonic strain, Δx ~1.8 %) of the CGO film in time, excited by a combined electric field [E_{AC} (16 kV/cm) + E_{DC} (0.8 MV/cm)] at 1 Hz. **(b)** The corresponding FFT amplitude spectrum of the first harmonic output electromechanical signals as a function of *f*. **(c)** A long-time (> 15 hours) output signal acquisition for the first harmonic piezoelectric displacement of the CGO film. This result shows excellent endurance of the piezoelectric performance of the CGO sample without significant signal degradation.

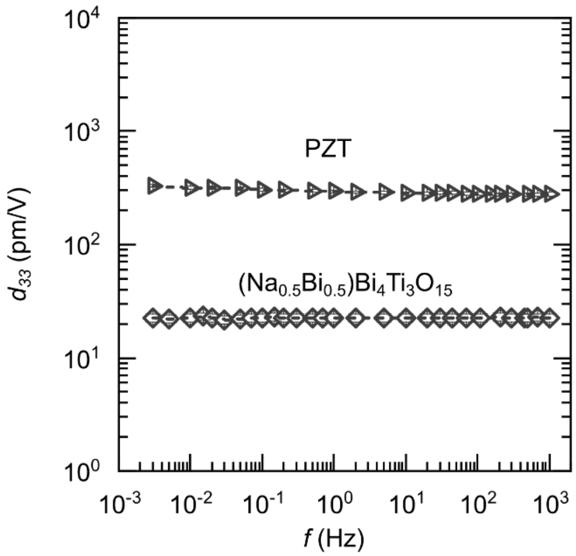

Fig. S9. Frequency-independent piezoelectric susceptibility of PZT and $(Na_{1/2}Bi_{1/2})Bi_4Ti_3O_{15}$- based material. Piezoelectric coefficients ($|d_{33}|$) of PZT and $(Na_{1/2}Bi_{1/2})Bi_4Ti_3O_{15}$ (PZ46-Ferropem) ceramics in the frequency range of 3 mHz – 1 kHz, measured by E_{AC} = 1.25 kV/cm.

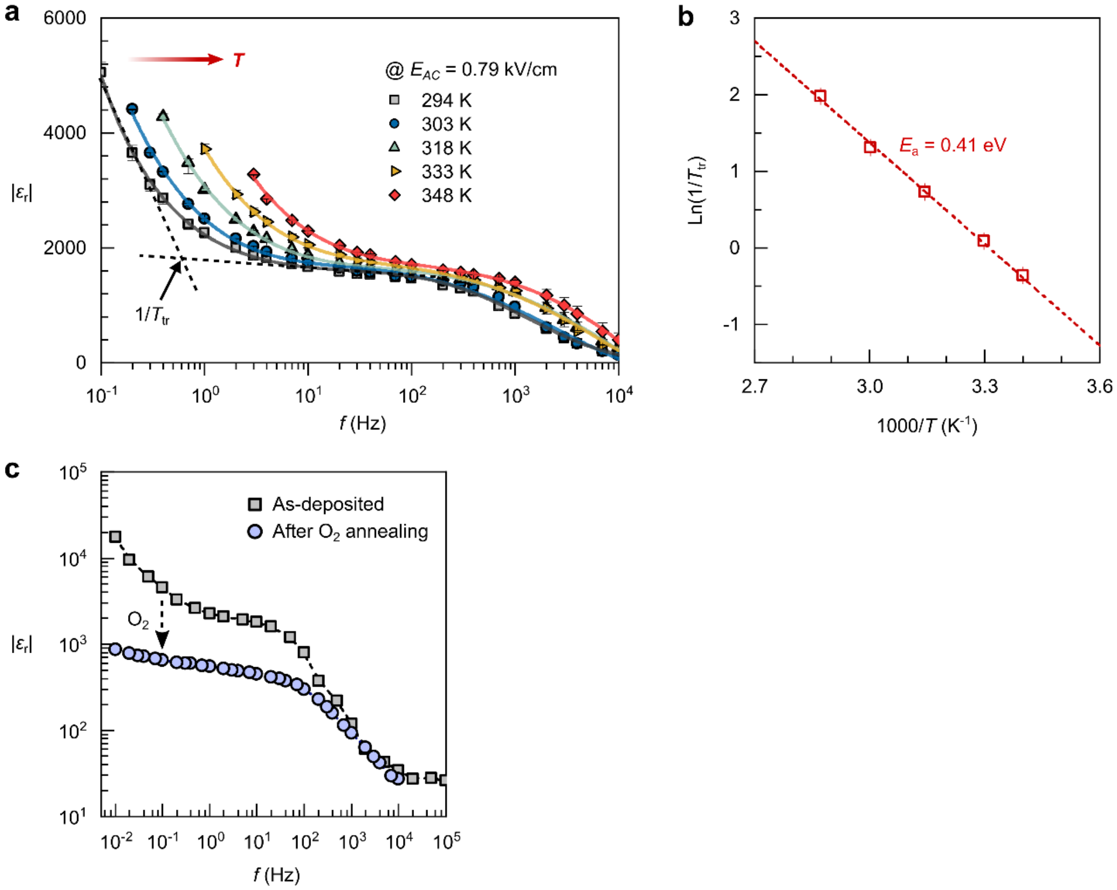

Fig. S10. Dielectric dispersion of CGO film with temperature variations. (a) Dielectric permittivity, ε_r, of the CGO film as a function of f, measured in the range of T = 294 – 348 K. Transient times, T_{tr}, for the characteristic dielectric relaxation in a CGO film were determined by linear extrapolation of the onsets to the plateaus. **(b)** an Arrhenius plot of $\mathrm{Ln}(1/T_{tr})$ in 1000/T. An activation energy of the T_{tr} was determined to be $E_a = 0.41 \pm 0.02$ eV. **(c)** ε_r of a CGO film as a function of frequency before and after O_2 annealing. The sample was annealed in O_2 flow at 400 °C for 30 mins. After annealing the permittivity decreases by more than an order of magnitude at low frequencies, indicating a large contribution of V_O to the permittivity and therefore piezoelectric properties at low frequencies.

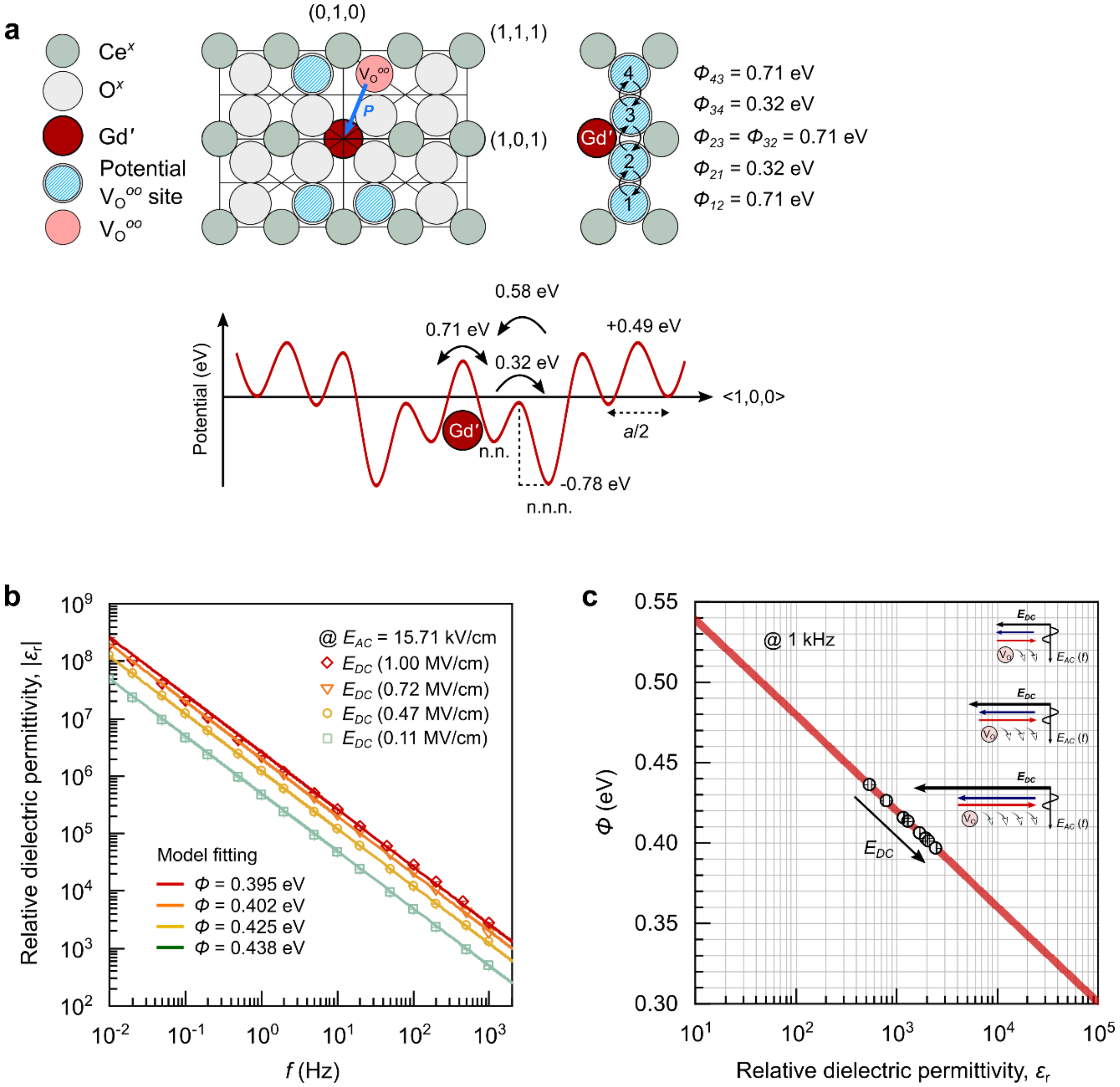

Fig. S11. Calculations on defect hopping, polarization, and dielectric constant of CGO (Gd 20%) system. (a) Schematics of polariztion between Gd dopant at coordinate (0,0,0) and next neighboring V_O at the coordinate (¼,¼,¼) in cubic fluorite CGO (Gd 20%) structure. On the right side, energetic description of V_O jumping processes in a simplified 4-oxygen site model. On the lower side, different energy potentials of V_O jumping at oxygen sites with respect to Gd site. This reveals preferential Vo hopping is along the next-next neighboring oxygen sites (¼, ¾, ¼). The values of oxygen hopping energies were referred to (*19*). **(b)** Fittings for the experimental frequency-dependent $|\varepsilon_r|$ of the CGO film, excited by simultaneous field application of a constant E_{AC} and different E_{DC} (0.11, 0.47, 0.72, and 1 MV/cm). The fittings are obtained using Eq. 3.10 with different values of Φ. **(c)** Experimental high-frequency (1 kHz) dielectric permittivity and the corresponding calculated Φ of the CGO film with different E_{DC}.

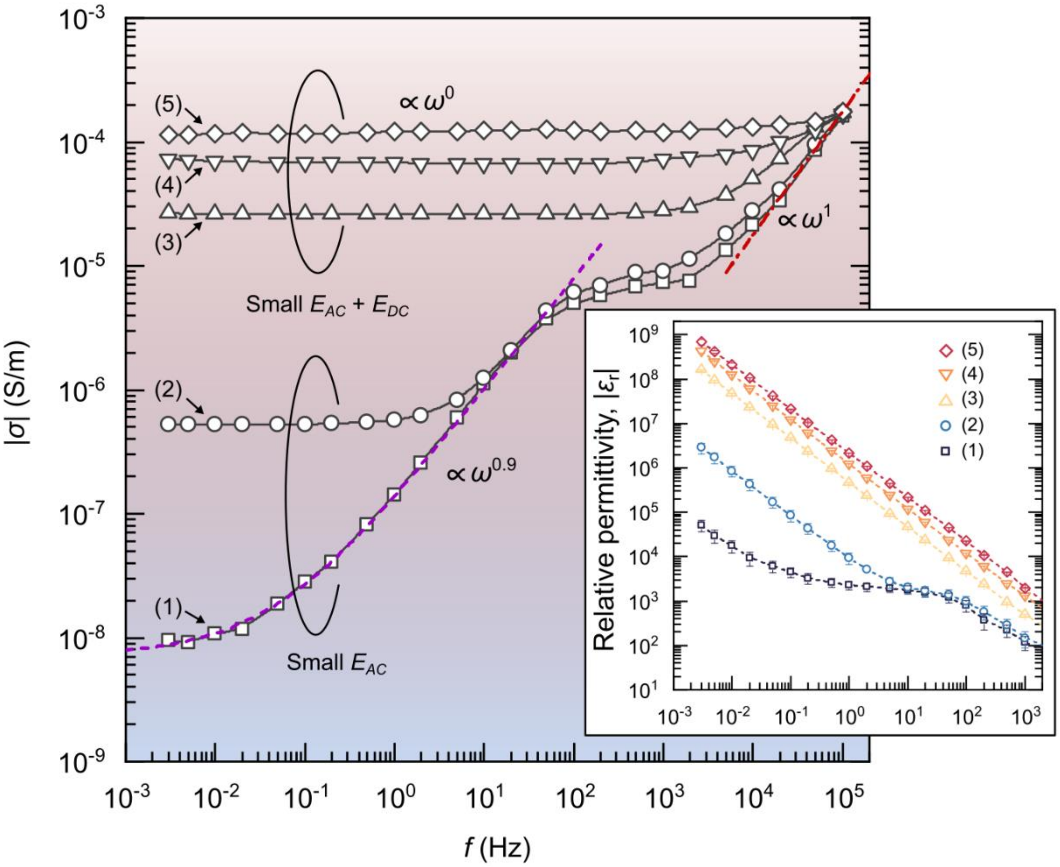

Fig. S12. Frequency-dependent electrical conductivity, $|\sigma| = \sqrt{\sigma'^2 + \sigma''^2} \approx \sigma'$, of a CGO (Gd 20%) film with different field excitations: (1) with E_{AC} = 0.79 kV/cm, (2) with E_{AC} = 15.71 kV/cm, (3) with E_{AC} = 15.71 kV/cm and E_{DC} = 0.11 MV/cm, (4) with E_{AC} = 15.71 kV/cm and E_{DC} = 0.47 MV/cm, and (5) with E_{AC} = 15.71 kV/cm and E_{DC} = 0.72 kV/cm. The dashed line represents an ionic relaxation behavior, expressed by $\sigma(\omega) = \sigma_0 + A\omega^n$, where σ_0 is the DC-conductivity (low-frequency), A is a temperature-related term and the exponent, n, lies in the range $0 < n < 1$. The dashed line with $n = 0.9$ in relatively low frequency range (< below 1 kHz) represents a dispersive ionic diffusion (*37*, *38*), while the line with $n = 1$ at high frequency range (> 1 kHz) represents a universal limiting conductivity (*39*). With simultaneous application of AC and DC fields to the sample, the Jonscher's power law is absent ($n \approx 0$) and frequency-independent DC-conductivity occurs, indicating greatly enhanced long-range ionic diffusion/hopping process (*40*). The inset shows the corresponding logarithmic $|\varepsilon_{\mathrm{r}}|(\sqrt{\varepsilon_{\mathrm{r}}'^2 + \varepsilon_{\mathrm{r}}''^2} \approx \varepsilon_{\mathrm{r}}'')$ versus logarithmic f for the excited CGO sample with different field applications (1 - 5).

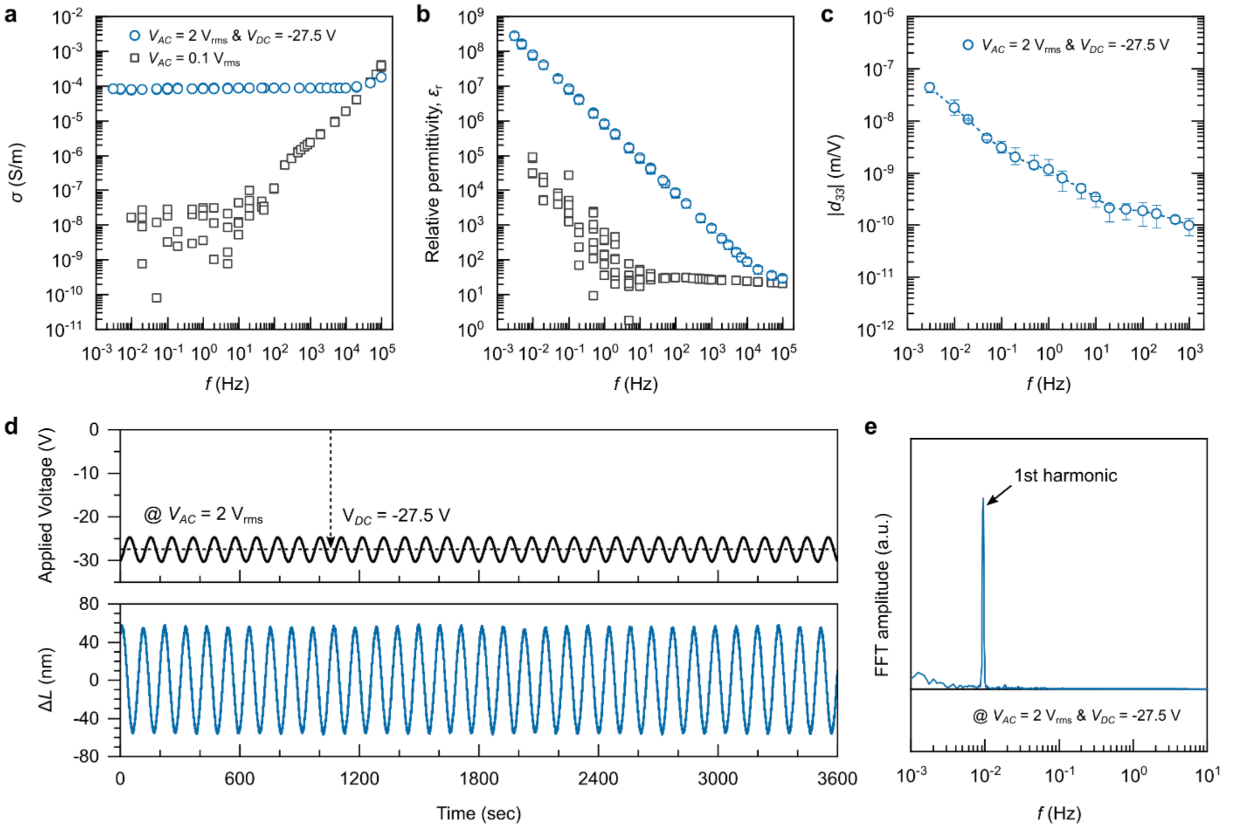

Fig. S13. Electrical conductivity, dielectric permittivity, and piezoelectricity in YSZ film. (a) Electrical conductivity versus frequency of a YSZ (Y 8 %) film (~300 nm), measured by AC 100 mV_{rms} (open square) and a simultaneous voltage application (AC 2 V_{rms} and DC -27.5 V). **(b)** Dielectric permittivity versus frequency of the YSZ film. **(c)** Frequency-dependent piezoelectric coefficient, d_{33}, of the YSZ film, excited by simultaneous application of AC 2 V_{rms} and DC -27.5 V. **(d)** The first-order electromechanical displacements of the YSZ film, excited by simultaneously applying AC 2 V_{rms} and DC -27.5 V (E_{DC} ~0.9 MV/cm), measured at about 10 mHz (9.4 mHz). **(e)** The corresponding FFT magnitude spectra of the output signals as a function of f.

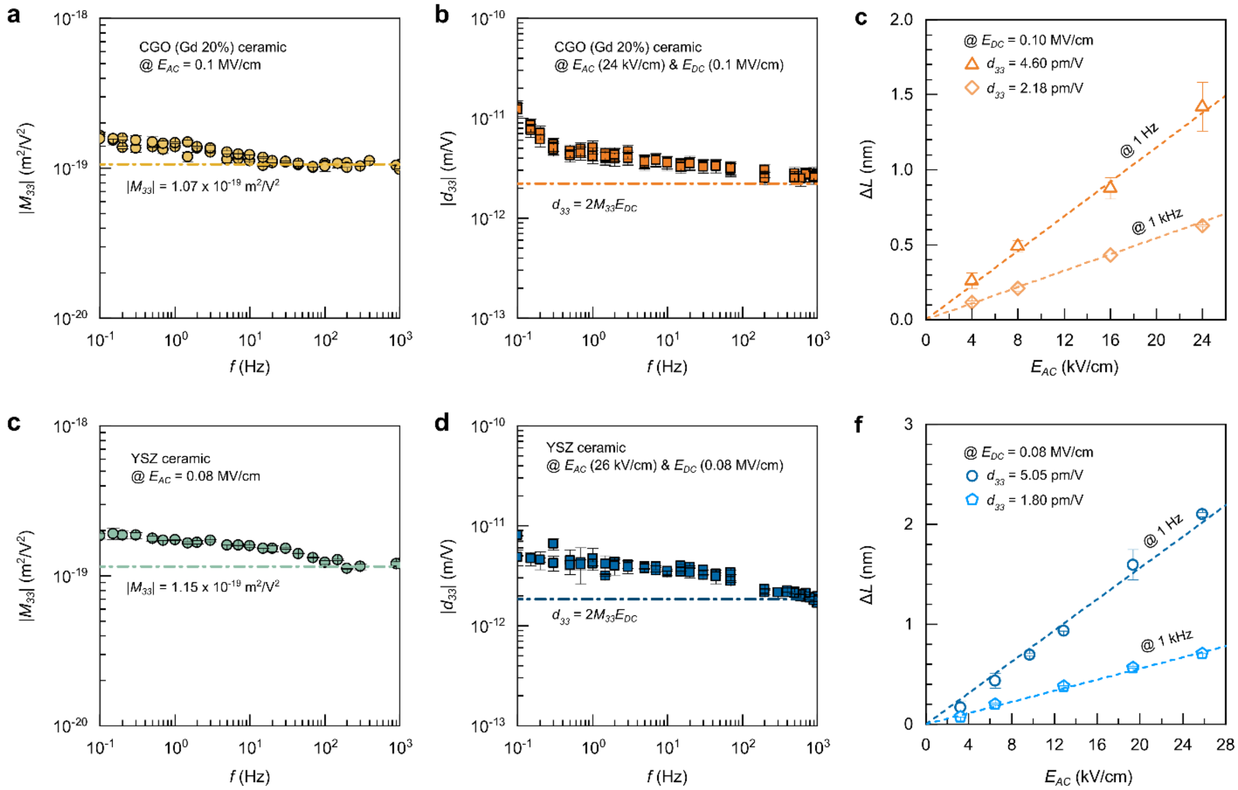

Fig. S14. Electrostriction and piezoelectricity in CGO and YSZ ceramics. (a) Frequency-dependent M_{33} of CGO ceramic, excited by E_{AC} = 0.1 MV/cm. **(b)** Frequency-dependent d_{33} of the CGO ceramic, excited by E_{AC} (24 kV/cm) + E_{DC} (0.1 MV/cm). **(c)** Linear piezoelectric displacements of the CGO ceramics under E_{DC} = 0.1 MV/cm, measured with various E_{AC} and at 1 Hz and 1 kHz. **(d)** Frequency-dependent M_{33} of YSZ ceramic, excited by E_{AC} = 0.08 MV/cm. **(e)** Frequency-dependent d_{33} of the YSZ ceramic, excited by E_{AC} (26 kV/cm) + E_{DC} (0.08 MV/cm). **(f)** Linear piezoelectric displacements of the YSZ ceramics under E_{DC} = 0.08 MV/cm, measured with various E_{AC} and at 1 Hz and 1 kHz. These results confirm that: (i) piezoelectricity in centrosymmetric fluorite oxide ceramics can be generated via our working concept (E_{AC} + E_{DC}), and (ii) high-frequency (1 kHz) piezoelectricity holds the relation of $d_{33} = 2M_{33}E_{DC}$.

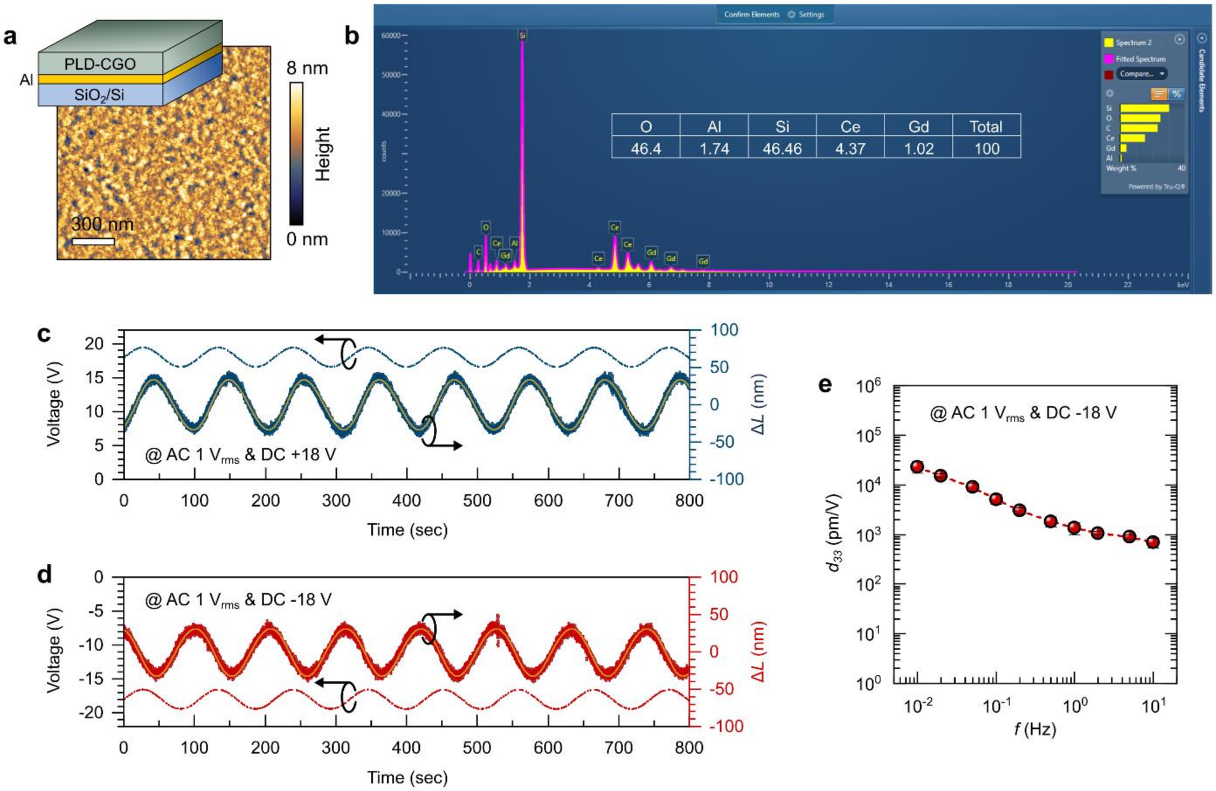

O	Al	Si	Ce	Gd	Total
46.4	1.74	46.46	4.37	1.02	100

Fig. S15. Induced piezoelectric effect in a RT-CGO film deposited by using pulsed laser deposition. (a) Surface morphology of a PLD-deposited polycrystalline CGO film (~350 nm) on Al (150 nm)/SiO_2 (150 nm)/Si substrate as schematically illustrated. **(b)** Energy dispersive X-ray spectroscopy analysis for the atomic composition of the PLD-deposited CGO sample. No impurities were found in the sample (detection limit <1%). **(c,d)** Reversible switching for the sign of piezoelectric displacements of the PLD-CGO sample with respect to the sign of the applied DC voltages (E_{DC} = ±0.51 MV/cm) while applying the same AC voltage (E_{AC} = 40.4 kV/cm). **(e)** Piezoelectric coefficients (d_{33}) of the PLD-deposited CGO film as a function of frequency, *f*. The observed frequency-dependent d_{33} is consistent with that observed in sputtered CGO and PLD-deposited YSZ. Therefore, we confirm that the fundamental mechanism and findings on the generation of the piezoelectricity in CGO are unaffected by Cr impurity.

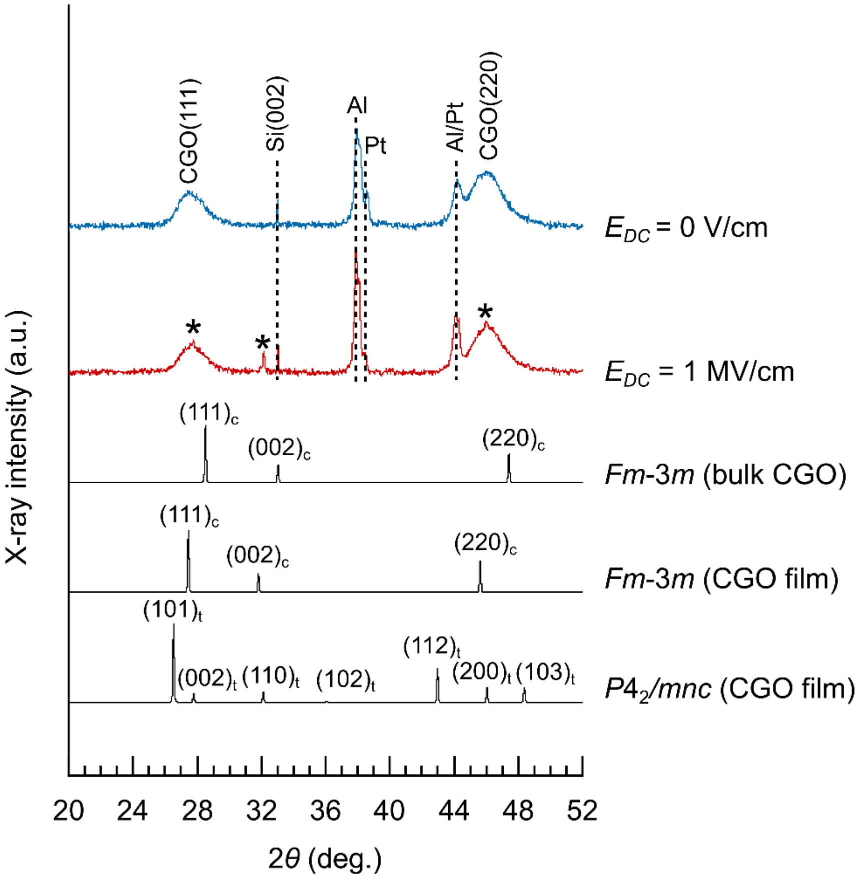

Fig. S16. In-situ x-ray diffraction measurements. XRD patterns of the CGO film with and without DC electric field application. The pristine polycrystalline CGO film predominantly shows broad (111) and (220) peaks at 2θ = 27.49° and 46.12°. Whilst, the new peaks visibly appear at 2θ = 27.78°, 32.16°, and 46.03° when E_{DC} (= 1 MV/cm) is applied to the CGO film.

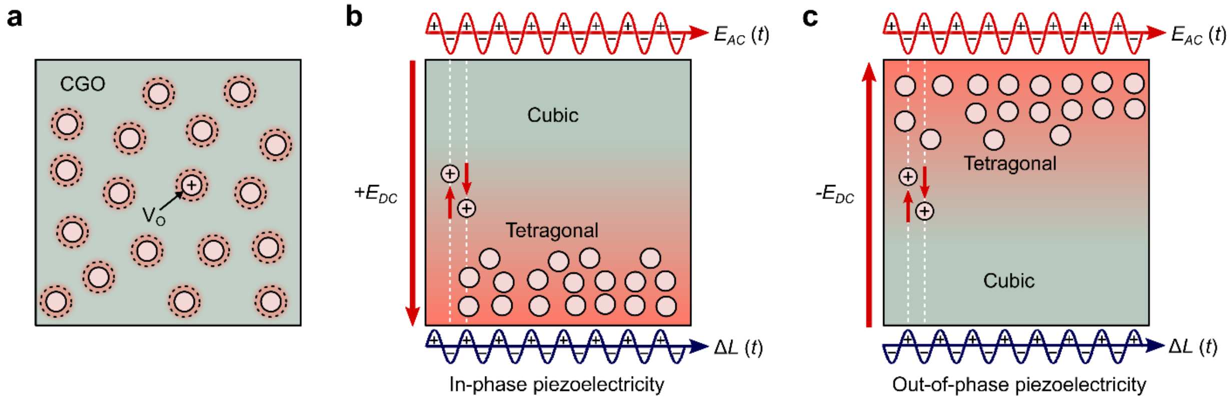

Fig. S17. Piezoelectric displacements of the CGO film via the control of electric field. (a) The pristine CGO film with a random distribution of oxygen vacancies (V_O). V_O-induced lattice distortions occur at the local areas of the film. **(b)** In-phase piezoelectric displacements, generated by applying E_{AC} under a concurrent positive E_{DC} (from the top to bottom electrodes). The piezoelectric displacement is determined by E_{AC} -driven V_O motion, i.e., more V_O towards the bottom electrode with positive E_{AC} for expansion, while less V_O towards the top electrode with negative E_{AC} for contraction. **(c)** Out-of-phase piezoelectric displacements, generated by applying E_{AC} under a concurrent negative E_{DC} (from the bottom to top electrodes). The piezoelectric displacement is also determined by E_{AC}-driven V_O motion, i.e., less V_O towards the bottom electrode with positive E_{AC} for contraction, while more V_O towards the top electrode with negative E_{AC} for expansion.

References and Notes

1. R. E. Newnham, *Properties of Materials: Anisotropy, Symmetry, Structure* (Oxford Univ. Press, 2005).

2. J. Holterman, P. Groen, *An Introduction to Piezoelectric Materials and Components* (Applied Piezo, 2012).

3. S.-E. Park, T. R. Shrout, Ultrahigh Strain and Piezoelectric Behavior in Relaxor Based Ferroelectric Single Crystals. *J. Appl. Phys.* **82**, 1804–1811 (1997). doi:10.1063/1.365983

4. F. Li, M. J. Cabral, B. Xu, Z. Cheng, E. C. Dickey, J. M. LeBeau, J. Wang, J. Luo, S. Taylor, W. Hackenberger, L. Bellaiche, Z. Xu, L.-Q. Chen, T. R. Shrout, S. Zhang, Giant piezoelectricity of Sm-doped $Pb(Mg_{1/3}Nb_{2/3})O_3$-$PbTiO_3$ single crystals. *Science* **364**, 264–268 (2019). doi:10.1126/science.aaw2781 Medline

5. H. Liu, H. Wu, K. P. Ong, T. Yang, P. Yang, P. K. Das, X. Chi, Y. Zhang, C. Diao, W. K. A. Wong, E. P. Chew, Y. F. Chen, C. K. I. Tan, A. Rusydi, M. B. H. Breese, D. J. Singh, L.-Q. Chen, S. J. Pennycook, K. Yao, Giant piezoelectricity in oxide thin films with nanopillar structure. *Science* **369**, 292–297 (2020). doi:10.1126/science.abb3209 Medline

6. B. Jaffe, W. R. Cook, H. L. Jaffe, *Piezoelectric Ceramics* (Academic Press, 1971).

7. J. Kuwata, K. Uchino, Sh. Nomura, Electrostrictive Coefficients of $Pb(Mg_{1/3}Nb_{2/3})O_3$ Ceramics. *Jpn. J. Appl. Phys.* **19**, 2099–2103 (1980). doi:10.1143/JJAP.19.2099

8. B. Khanbabaee, E. Mehner, C. Richter, J. Hanzig, M. Zschornak, U. Pietsch, H. Stocker, T. Leisegang, D. C. Meyer, S. Gorfman, Large Piezoelectricity in Electric-Field Modified Single Crystals of $SrTiO_3$. *Appl. Phys. Lett.* **109**, 222901 (2016). doi:10.1063/1.4966892

9. M.-M. Yang, Z.-D. Luo, Z. Mi, J. Zhao, S. P. e, M. Alexe, Piezoelectric and pyroelectric effects induced by interface polar symmetry. *Nature* **584**, 377–381 (2020). doi:10.1038/s41586-020-2602-4 Medline

10. J. G. Swallow, J. J. Kim, J. M. Maloney, D. Chen, J. F. Smith, S. R. Bishop, H. L. Tuller, K. J. Van Vliet, Dynamic chemical expansion of thin-film non-stoichiometric oxides at extreme temperatures. *Nat. Mater.* **16**, 749–754 (2017). doi:10.1038/nmat4898 Medline

11. R. Korobko, A. Patlolla, A. Kossoy, E. Wachtel, H. L. Tuller, A. I. Frenkel, I. Lubomirsky, Giant electrostriction in Gd-doped ceria. *Adv. Mater.* **24**, 5857–5861 (2012). doi:10.1002/adma.201202270 Medline

12. A. Kossoy, Q. Wang, R. Korobko, V. Grover, Y. Feldman, E. Wachtel, A. K. Tyagi, A. I. Frenkel, I. Lubomirsky, Evolution of the Local Structure at the Phase Transition in CeO_2-Gd_2O_3 Solid Solutions. *Phys. Rev. B* **87**, 054101 (2013). doi:10.1103/PhysRevB.87.054101

13. R. Schmitt, A. Nenning, O. Kraynis, R. Korobko, A. I. Frenkel, I. Lubomirsky, S. M. Haile, J. L. M. Rupp, A review of defect structure and chemistry in ceria and its solid solutions. *Chem. Soc. Rev.* **49**, 554–592 (2020). doi:10.1039/C9CS00588A Medline

14. M. Hadad, H. Ashraf, G. Mohanty, C. Sandu, P. Muralt, Key-Features in Processing and Microstructure for Achieving Giant Electrostriction in Gadolinium Doped Ceria Thin Films. *Acta Mater.* **118**, 1–7 (2016). doi:10.1016/j.actamat.2016.07.025

15. N. Setter, D. Damjanovic, L. Eng, G. Fox, S. Gevorgian, S. Hong, A. Kingon, H. Kohlstedt, N. Y. Park, G. B. Stephenson, I. Stolitchnov, A. K. Tagantsev, D. V. Taylor, T. Yamada, S. Streiffer, Ferroelectric Thin Films: Review of Materials, Properties and Applications. *J. Appl. Phys.* **100**, 051606 (2006). doi:10.1063/1.2336999

16. Materials and methods are available as supplementary materials online.

17. R. E. Newnham, V. Sundar, R. Yimnirun, J. Su, Q. M. Zhang, Electrostriction: Nonlinear Electromechanical Coupling in Solid Dielectrics. *J. Phys. Chem. B* **101**, 10141–10150 (1997). doi:10.1021/jp971522c

18. F. A. Kröger, H. J. Vink, Relations between the concentrations of imperfections in crystalline solids. *Solid State Phys.* **3**, 307–435 (1956). doi:10.1016/S0081-1947(08)60135-6

19. J. Faber, C. Geoffroy, A. Roux, A. Sylvestre, P. Abélard, A Systematic investigation of the dc electrical conductivity of rare-earth doped ceria. *Appl. Phys. A* **49**, 225–232 (1989). doi:10.1007/BF00616848

20. D. Marrocchelli, S. R. Bishop, H. L. Tuller, B. Yildiz, Understanding Chemical Expansion in Non-Stoichiometric Oxides: Ceria and Zirconia Case Studies. *Adv. Funct. Mater.* **22**, 1958–1965 (2012). doi:10.1002/adfm.201102648

21. A. S. Nowick, W. R. Heller, Dielectric and Anelastic Relaxation of Crystals Containing Point Defects. *Adv. Phys.* **14**, 101–166 (1965). doi:10.1080/00018736500101021

22. A. Lai, C. A. Schuh, Direct Electric-Field Induced Phase Transformation in Paraelectric Zirconia via Electrical Susceptibility Mismatch. *Phys. Rev. Lett.* **126**, 015701 (2021). doi:10.1103/PhysRevLett.126.015701 Medline

23. B. D. C. Bell, S. T. Murphy, P. A. Burr, R. W. Grimes, M. R. Wenman, Accommodation of Tin in Tetragonal ZrO_2. *J. Appl. Phys.* **117**, 084901 (2015). doi:10.1063/1.4909505

24. H. Ikeno, M. Krause, T. Höche, C. Patzig, Y. Hu, A. Gawronski, I. Tanaka, C. Rüssel, Variation of Zr-$L_{2,3}$ XANES in tetravalent zirconium oxides. *J. Phys. Condens. Matter* **25**, 165505 (2013). doi:10.1088/0953-8984/25/16/165505 Medline

25. H. Zhu, C. Yang, Q. Li, Y. Ren, J. C. Neuefeind, L. Gu, H. Liu, L. Fan, J. Chen, J. Deng, N. Wang, J. Hong, X. Xing, Charge transfer drives anomalous phase transition in ceria. *Nat. Commun.* **9**, 5063 (2018). doi:10.1038/s41467-018-07526-x Medline

26. G. S. Radchenko, A. V. Turik, Giant Piezoelectric Effect in Layered Ferroelectric-Polymer Composites. *Phys. Solid State* **45**, 1759–1762 (2003). doi:10.1134/1.1611247

27. P. P. Dholabhai, J. B. Adams, P. Crozier, R. Sharma, Oxygen vacancy migration in ceria and Pr-doped ceria: A DFT+U study. *J. Chem. Phys.* **132**, 094104 (2010). doi:10.1063/1.3327684 Medline

28. D. Kek-Merl, J. Lappalainen, H. L. Tuller, Electrical Properties of Nanocrystalline CeO_2 Thin Films Deposited by in situ Pulsed Laser Deposition. *J. Electrochem. Soc.* **153**, J15 (2006). doi:10.1149/1.2165778

29. A. Tschöpe, R. Birringer, Grain size dependence of electrical conductivity in polycrystalline cerium oxide. *J. Electroceram.* **7**, 169–177 (2001). doi:10.1023/A:1014483028210

30. M. Alaydrus, M. Sakaue, H. Kasai, A DFT+*U* study on the contribution of 4f electrons to oxygen vacancy formation and migration in Ln-doped CeO_2. *Phys. Chem. Chem. Phys.* **18**, 12938–12946 (2016). doi:10.1039/C6CP00637J Medline

31. P. Zaumseil, High-resolution characterization of the forbidden Si 200 and Si 222 reflections. *J. Appl. Cryst.* **48**, 528–532 (2015). doi:10.1107/S1600576715004732 Medline

32. P. K. Schelling, S. R. Phillpot, D. Wolf, Mechanism of the Cubic-to-Tetragonal Phase Transition in Zirconia and Yttria-Stabilized Zirconia by Molecular-Dynamics Simulation. *J. Am. Ceram. Soc.* **84**, 1609–1619 (2001). doi:10.1111/j.1151-2916.2001.tb00885.x

33. W. Pan, Q. Zhang, A. S. Bhalla, L. E. Cross, Field-Induced Strain in Single-Crystal $BaTiO_3$. *J. Am. Ceram. Soc.* **71**, C-302–C-305 (1988). doi:10.1111/j.1151-2916.1988.tb05909.x

34. M. E. Lines, A. M. Glass, *Principles and Applications of Ferroelectrics and Related Materials* (Oxford Univ. Press, 1979).

35. H. Hayashi, M. Kanoh, C. J. Quan, H. Inaba, S. Wang, M. Dokiya, H. Tagawa, Thermal Expansion of Gd-doped Ceria and Reduced Ceria. *Solid State Ion.* **132**, 227–233 (2000). doi:10.1016/S0167-2738(00)00646-9

36. A. R. von Hippel, *Dielectrics and Waves* (MIT Press, 1954).

37. A. K. Jonscher, The ‘Universal’ Dielectric Response. *Nature* **267**, 673–679 (1977). doi:10.1038/267673a0

38. A. K. Jonscher, The Physical Origin of Negative Capacitance. *J. Chem. Soc. Faraday Trans. 2* **82**, 75–81 (1986). doi:10.1039/f29868200075

39. W. K. Lee, J. F. Liu, A. S. Nowick, Limiting behavior of ac conductivity in ionically conducting crystals and glasses: A new universality. *Phys. Rev. Lett.* **67**, 1559–1561 (1991). doi:10.1103/PhysRevLett.67.1559 Medline

40. J. Garcia-Barriocanal, A. Rivera-Calzada, M. Varela, Z. Sefrioui, E. Iborra, C. Leon, S. J. Pennycook, J. Santamaria, Colossal ionic conductivity at interfaces of epitaxial ZrO_2:$Y2O_3$/$SrTiO_3$ heterostructures. *Science* **321**, 676–680 (2008). doi:10.1126/science.1156393 Medline